ACS APPLIED ENERGY MATERIALS

www.acsaem.org Article

$Hf_2B_2Ir_5$: A Self-Optimizing Catalyst for the Oxygen Evolution Reaction

Ana M. Barrios Jiménez, Ulrich Burkhardt, Raul Cardoso-Gil, Katharina Höfer, Simone G. Altendorf, Robert Schlögl, Yuri Grin,* and Iryna Antonyshyn*

Cite This: *ACS Appl. Energy Mater.* 2020, 3, 11042−11052 Read Online

ACCESS | Metrics & More | Article Recommendations | Supporting Information

ABSTRACT: The ternary compound $Hf_2B_2Ir_5$ was assessed as an electrocatalyst for the oxygen evolution reaction (OER) in 0.1 M H_2SO_4. The oxidative environment restructures the studied material in the near-surface region, creating cavities in which agglomerates of $IrO_x(OH)_y(SO_4)_z$ particles are incorporated. These in situ generated particles result from the oxidation of secondary phases in the matrix as well as from self-controlled near-surface oxidation of the ternary compound itself. The oxidation is controlled by the structural and chemical bonding features of $Hf_2B_2Ir_5$. The cage-like motif, exhibiting mostly ionic interactions between positively charged Hf atoms and a covalently bonded Ir−B network, selectively controls the extent and kinetics of the transformation process induced during the operation of the electrocatalyst. The resulting self-optimized composite material, formed by a $Hf_2B_2Ir_5$ matrix surrounding $IrO_x(OH)_y(SO_4)_z$ particles, was used in the OER over 240 h at 100 mA cm^{-2} current density. The chemical changes, as well as the OER performance, were studied via a combination of bulk- and surface-sensitive experimental techniques as well as by employing a quantum-chemical bonding analysis.

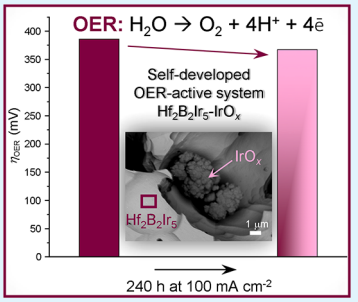

KEYWORDS: *energy conversion, oxygen evolution reaction (OER), acidic media, intermetallic compound, iridium, chemical bonding, surface oxidation*

INTRODUCTION

The need to replace fossil fuels by renewable alternatives is certainly not under question anymore.[1−3] Hydrogen is a critical component of future energy systems[4−6] and is accessible in the required amounts by water splitting (considering present oil and gas use).[7,8] The whole process is limited by the formation of oxygen, which requires the transfer of four electrons per product molecule,[9−12] leading to a reaction network of intermediates that must be controlled by suitably active and stable catalysts. Practical operation conditions further require high electronic conductivity of the electrode to minimize ohmic losses through the reactive interface. Additional challenges in the development and application of proton exchange membrane (PEM) electrolysis are associated with oxidative conditions of a strong acid, saturated with oxygen and products of the reaction network (OH, H_2O_2, HO_2), which the catalysts need to endure. Keeping in mind the thermodynamic instability of many transition metals in acidic solutions at applied anodic potentials,[13,14] there are not many electrocatalysts that are able to operate under such harsh oxygen evolution reaction (OER) conditions. Therefore, noble metals and their oxides as anode materials are still materials of choice.[10,15−17]

Among the large number of materials studied, none can compete with iridium and its oxides, which exhibit both outstanding activity and sufficient stability for technological applications.[18−24] The scarcity of Ir prevents its application on the scale required for global hydrogen production. To exploit the inherent advantages of acid electrolysis, the replacement of Ir_xO_y (or at least reduction of the Ir amount) is necessary. As one of the possible strategies for the material search, the modification of the electronic structure by changing the composition and crystal structure can be considered.[11,25−27] Intermetallic compounds (IMCs), in contrast to substitutional alloys, offer many advantages for the design of electrodes, for instance, well-ordered atomic arrangements with directed covalent interactions, the tunable coordination environment of noble metals, and hence existence of hierarchical cluster structures combining elements with diverging chemical properties in one single phase.[28−31] Reports on the application of intermetallic compounds for the OER are scarce in the literature and limited to a few examples, among which binary compounds Ni_2Ta[32] and Al_2Pt[33] have been investigated recently.

The concept of the present work is to dilute Ir atoms in a well-defined chemically robust coordination environment bringing about an electronic structure with low electron

Received: August 20, 2020
Accepted: October 7, 2020
Published: October 21, 2020

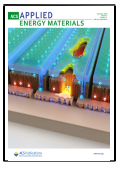

https://dx.doi.org/10.1021/acsaem.0c02022
ACS Appl. Energy Mater. 2020, 3, 11042−11052

density around the Ir as required to form the active IrOOH component. The result is the IMC $Hf_2B_2Ir_5$. The choice of Ir followed its unprecedented performance in the OER, and it allows carrying out the proof-of-principle study. It is expected that activation of the initial IMC phase needs to occur to generate the active sites binding water to the surface of the electron-deficient electrode. The work describes how this activation occurs and whether the covalent−ionic mixed bonding scheme will lead to a self-limitation of the activation, preserving the metallic core of the non-metallic electrode surface.

To the best of our knowledge, neither hafnium nor boron was mentioned in the literature as active components for the OER, but both should contribute to the enhanced stability of the investigated catalytic material (cf. e.g., thermal stability of binary hafnium borides with the formation temperatures of 3380 °C for HfB_2 or 2120 °C for HfB).[34] There are no published data on Hf-based compounds as OER electrocatalysts in acidic media. Nevertheless, during the last few decades, they have attracted interest as electrocatalysts for other half-reactions of water splitting: e.g., HfO_xN_y (acidic ORR,[35] HER, and HOR[36]), HfB_2 (acidic HER and alkaline ORR[37]), and solid solution HfB_2-ZrB_2 (acidic and alkaline HER[38]). The compounds Hf_2Fe, Hf_2Co, and Hf_2Ni were investigated as possible hydrogen storage materials, and their application as electrode materials was also mentioned, but no details were published.[39] The limited application of Hf-based compounds (e.g., diboride) can be related to their restricted chemical stability in acidic media.[40]

Addressing the knowledge about the application of borides for the OER, a few important issues need to be highlighted: (i) borides are known as active and stable electrocatalysts for the OER only (!) in alkaline media;[41−48] (ii) numerous works on borides in alkaline media are mainly focused on activity; however, a clear vision about the role of boron is extremely limited; and (iii) the formation of surface oxide/hydroxide under reaction conditions remains the dominant criterion for activity determination.[46,49,50] From this knowledge, it occurs that Ir in the present case is not only the precursor of the active sites but also contributes to the chemical stability of the Hf−Ir−B moiety. Complete inertness of the matrix to reaction conditions is not desired as it would minimize the ability of the system to be activated into a state different from the surface resulted from the bulk synthesis procedure.

Several questions, arising from the concept outlined, will be addressed in this work: (i) activity of intermetallic compound $Hf_2B_2Ir_5$ as the electrocatalyst for the OER; (ii) chemical changes in the near-surface region under oxidative conditions; (iii) relationship of the material changes to the features of chemical bonding, and (iv) rationalization of the electrocatalytic performance of the investigated compound through its ability to self-activate under reaction conditions.

EXPERIMENTAL SECTION

Sample Preparation. For material synthesis, a Hf rod (Haines & Maassen GmbH, 99.9%), Ir powder (ChemPUR, 99.9%), and B crystalline powder (ChemPUR, 99.99%) were used. The synthesis was carried out in three steps: (i) preparation of the Ir−B precursor (the powders of Ir and B were pressed into a pellet and annealed at 1270 K for 4 days); (ii) Hf pieces and Ir−B precursor were arc-melted under an Ar atmosphere on a water-cooled copper bottom with mass losses less than 2%; and (iii) homogenization heat treatment was performed between 1470 and 1570 K for several weeks. To obtain the specimen for electrochemical experiments, the sample was ground in an agate mortar and filled into a carbon pressform. The densification was performed via spark plasma sintering (SPS) by heating up to 1270 K at a rate of 10 K min^{-1} with subsequent cooling down to room temperature. After SPS, pellets were polished in three stages: (1) manually with SiC grinding papers (Grit 100, 400, and 500); (2) via contact with a rotating plate with SiC grinding papers (Grit 800, 1200, 2400, and 4000 at 250 rpm) on polishing device LaboPol-21, and (3) final polishing with diamond solution (diamond particle size 3, 1, and 1/4 μm) and water-based green lubricant (Struers GmbH) on an MD-Dur plate (made of satin woven natural silk) at 800 rpm on a polishing machine RotoPol-15.

Material Characterization. X-ray powder diffraction patterns were collected either in transmission mode on a Huber G670 imaging-plate Guinier camera for powdered samples or in reflection geometry on an STOE STADIP MP diffractometer, equipped with a DECTRIS MYTHEN 1K detector for compacted samples. In both cases, Cu Kα_1 radiation (λ = 1.54059 Å) was used. The phase analysis was performed via the comparison of experimental powder X-ray diffraction (PXRD) patterns with the calculated ones using WinXPOW software.[51] Lattice parameters were determined employing the software package WinCSD,[52] for the calibration of the peak positions, the LaB_6 (a = 4.1569 Å) was used as an internal standard.

Scanning electron microscopy (SEM) using a JEOL JSM-7800F microscope with an energy-dispersive X-ray spectroscopy (EDXS) system (Quantax 400, Bruker, Silicon Drift Detector) was employed to control the quality and homogeneity of the as-prepared sample as well as to monitor the changes after long-term electrochemical treatment. To highlight the bulk features, SEM data were collected with the acceleration voltages of 15−25 kV, whereas to check the changes in the near-surface region, this was reduced down to 5 kV. As a result, the semi-quantitative Hf/Ir ratios were obtained for different areas of the specimen as well as the morphology of the surface was screened using backscattered electron (BSE) and secondary electron (SE) images. Electron backscatter diffraction (EBSD) data were collected for the monitoring of possible preferential orientation of crystallites. For accurate composition determination, wavelength-dispersive X-ray spectroscopy (WDXS, CAMECA electron microprobe SX100 setup, tungsten cathode, elemental Ir and HfB_2 as reference materials) was carried out.

To determine the chemical state of the elements in initial and electrochemically treated specimens, X-ray photoelectron spectroscopy (XPS) was employed. The measurements were performed using a Vacuum Generators twin crystal monochromatized Al Kα ($h\nu$ = 1486.6 eV) source and a Scienta R3000 electron energy analyzer in normal emission geometry and at room temperature. The overall energy resolution was ∼0.4 eV, and the Fermi level was calibrated using a polycrystalline Ag reference. The pressure in the spectrometer chamber was in the low 10^{-10} mbar range.

Electrochemical Experiments. All electrochemical experiments were performed in a three-compartment electrochemical cell using a Biologic SP-300 potentiostat. A Pt wire electrode (PINE, 99.99%, 0.5 mm in diameter) and saturated calomel electrode (PINE, Hg/Hg_2Cl_2, 4 M KCl) were used as the counter and reference electrodes, respectively. The densified specimen of $Hf_2B_2Ir_5$ was used as a working electrode. Measurements were performed in Ar-saturated 0.1 M H_2SO_4 solution (prepared from concentrated H_2SO_4 (Alfa Aesar, 99.999%) and Millipore water 18.2 MΩ cm). Purging with argon (purity grade 5.0) was carried out for 30 min prior to each experiment. To pretreat the surface of the WE, cyclic voltammetry (CV) was performed (maximum potential (E_{max}) of 1.0 V_{RHE}; sweep rate of 50 mV s^{-1}; 50 cycles). Linear sweep voltammetry (LSV) was employed (E_{max} = 2.0 V_{RHE}; sweep rate of 5 mV s^{-1}) to evaluate the electrochemical activity. A long-term stability test was accomplished applying the chronopotentiometry (CP) technique (current density (j) of 100 mA cm^{-2}; duration 240 h). LSVs were recorded every 8 h to monitor the changes in the activity of the electrocatalyst during this experiment.

The current densities were normalized to the geometrical area of the pellets (0.204 cm^2). All values of potentials were IR-corrected and expressed versus the reference hydrogen electrode (RHE). The

https://dx.doi.org/10.1021/acsaem.0c02022
ACS Appl. Energy Mater. 2020, 3, 11042−11052

concentrations of the dissolved elements were determined by taking electrolyte aliquots at the end of the electrochemical experiment. Two electrolyte probes of 7 mL each were analyzed via inductively coupled plasma-optical emission spectrometry, ICP-OES 5100 SVDV (Agilent). The aliquots were handled without dilution since the obtained concentrations did not exceed the maximal value of the linear calibration. The calibration was performed using a six-point standard calibration series and blank probe of 0.1 M H_2SO_4.

RESULTS AND DISCUSSION

The ternary compound $Hf_2B_2Ir_5$ (more precisely $Hf_2B_{2-2x}Ir_{5+x}$) crystallizes with an own structure type (space group *Pbam*, a = 5.6218(2) Å, b = 11.2456(3) Å, c = 3.8292(1) Å, Figure 1).[53]

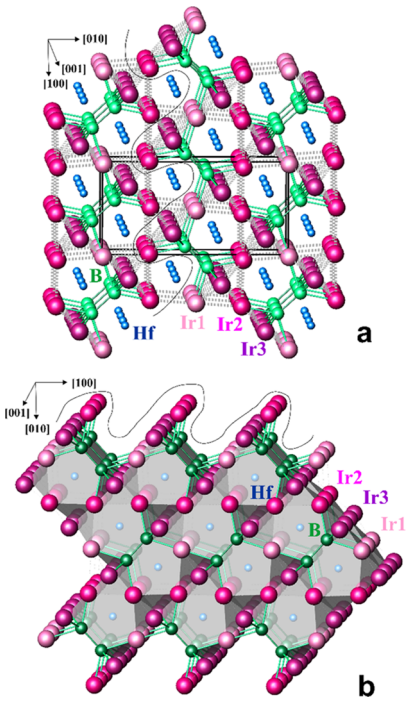

Figure 1. Chemical bonding and atomic arrangements in $Hf_2B_2Ir_5$: (a) Anionic groups B_2Ir_8 are built by covalent B−B and Ir−B interactions (green) and form two-dimensional layers parallel to the (010) plane sharing the Ir1 and Ir3 atoms; the layers are interconnected by two- and three-center Ir−Ir bonds (gray dash) to the three-dimensional framework. (b) Hafnium-centered 14-vertex cages within the framework (gray shapes) and atomic arrangements on the (010) surface formed by breaking the Ir−Ir interactions in the framework (wavy line).

Analysis of the chemical bonding reveals the B_2Ir_8 groups as the basic building unit of the crystal structure. The unit itself is held together by two-center B−B, two-center B−Ir1, and three-center Ir1−B−Ir3 and Ir2−B−Ir3 interactions (Figure 1, green lines). Sharing the Ir1 and Ir3 atoms, the B_2Ir_8 units form two-dimensional layers parallel to the (010) plane (Figure 1a). The layers are interconnected by two- and three-center Ir−Ir interactions (with small bonding populations) to a three-dimensional polyanionic framework. The latter bears hafnium cations in the cages with 14 vertices (Figure 1b).[53] Assuming that the Ir−Ir bonds are easier to break (waved line in Figure 1), the hafnium atoms can leave the solid, and the remaining (010) surface may be formed by the B_2Ir_8 units (Figure 1b). Such unique covalently bonded Ir−B fragments make the ternary compound $Hf_2B_2Ir_5$ attractive among other compounds in the Hf−B−Ir system in terms of catalyst stability under oxidative conditions. The Hf is not only critical in keeping the structure intact but also responsible for the formation of an Ir−B termination, out of which the IrOOH active phase may evolve in a controlled way.

Prior to the assessment of its electrochemical activity, the detailed characterization of the $Hf_2B_2Ir_5$ material via bulk-sensitive techniques was carried out. The powder X-ray diffraction pattern of the initial material reveals, besides a well-developed pattern of the desired $Hf_2B_2Ir_5$ phase, the presence of weak additional reflections, which is a hint of a minority phase in the synthesized sample (Figure 2). The

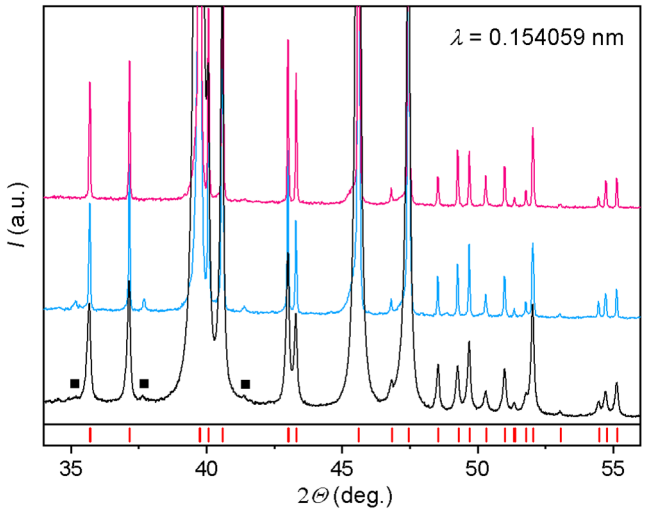

Figure 2. Powder X-ray diffraction patterns of $Hf_2B_2Ir_5$: as-synthesized (black), after CV (blue), and after long-term CP experiment (magenta). The red ticks show the positions of PXRD peaks for the main $Hf_2B_2Ir_5$ phase. The reflections of low intensity are assigned to traces of HfB_4Ir_3 and are marked by black squares.

attempts to ascribe these reflections to known binary and ternary compounds lead to the identification of HfB_4Ir_3.[54,55] Since the intensities of additional peaks are less than 2% from the maximum peak intensity of the main phase $Hf_2B_2Ir_5$, the minority phase HfB_4Ir_3 can be identified only by the assignment of its three (111), (201), and (300) most intense peaks (black squares in Figure 2).

Wavelength-dispersive X-ray spectroscopy (WDXS) reveals the matrix phase with elemental composition $Hf_{21.6(4)}B_{27.2(5)}Ir_{51.2(6)}$. These composition data deviate slightly from the intended $Hf_2B_2Ir_5$ values, mainly because of the uncertainty in the quantification of the boron content. However, the ratio of Hf/Ir is close to the expected 2:5. Furthermore, metallographic characterization confirms the presence of traces of a secondary phase (dark gray inclusions, Figure 3a,b). This phase contains less hafnium and is richer in iridium compared to the main phase $Hf_2B_2Ir_5$ (Figure S1). Further quantification is not possible due to the small grain size, but qualitative analysis clearly shows the presence of three constituent elements, revealing that the secondary phase belongs to the ternary Hf−B−Ir system. Furthermore, elemental mapping clearly shows the slight compositional difference in the regions of this admixture, which can be a sign of the second impurity, identification of which is hampered by very small amount and close compositions (Figure 3c). Thus, the material prepared for the electrochemical study is the

https://dx.doi.org/10.1021/acsaem.0c02022
ACS Appl. Energy Mater. 2020, 3, 11042−11052

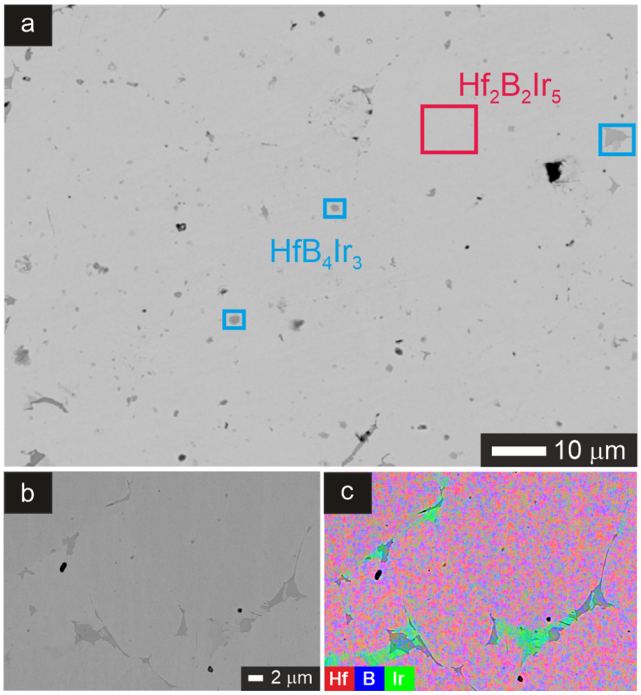

Figure 3. SEM of the sintered $Hf_2B_2Ir_5$ specimen (material contrast, 15 kV): (a) BSE image, showing the phases distribution over the sample; (b) enlargement of specimen region, containing the secondary phase; and (c) elemental mapping, revealing the presence of two secondary phases (light and dark green) with close compositions.

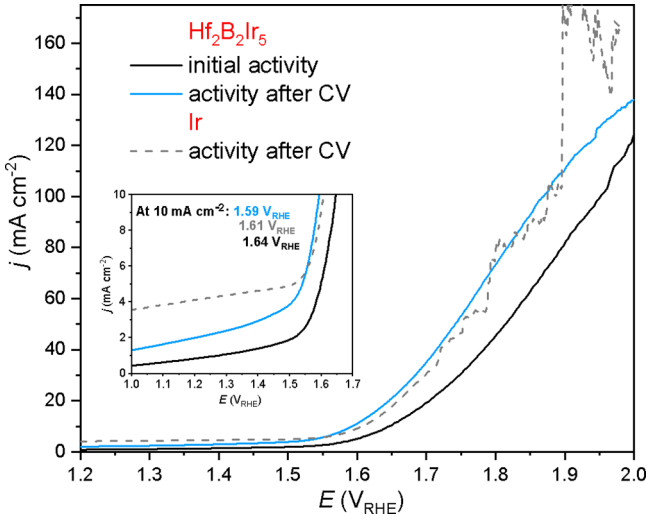

Figure 4. Linear sweep voltammetry of the $Hf_2B_2Ir_5$ working electrode: initial material (black solid) and after 50 CV cycles (blue solid) compared to elemental Ir (gray dashed). Inset: region of low current densities (j = 0−10 mA cm^{-2}) with highlighted OER onset potentials.

$Hf_2B_2Ir_5$ compound with minor (less than 1 vol %) inclusions of HfB_4Ir_3.

The first electrochemical cycle is of great importance since the OER at high anodic potentials enables the activation process with complex oxidation and surface modifications. This activation process should be taken into account during the discussion and comparison of the obtained results.[16,17] The initial electrochemical activity of $Hf_2B_2Ir_5$ was estimated from linear sweep voltammetry (LSV) data (Figure 4). The potential necessary to obtain a current density of 10 mA cm_{geom}^{-2}, is used as a benchmark value of OER activity at the level of fundamental studies.[56,57] In the electrochemical system with $Hf_2B_2Ir_5$ as the working electrode, this value was reached at 1.64 V_{RHE}, which is close to that of metallic Ir (10 mA cm_{geom}^{-2} at 1.61 V_{RHE}) following its activation to Ir^{III} oxyhydroxide.[21]

After the initial activity measurement, cyclic voltammetry (CV) was applied from +0.05 to +1.0 V_{RHE} (50 cycles, 50 mV s^{-1}). The maximum potential and appropriate scan rate were chosen based on surface redox electrochemical data for metallic Ir.[16,19,58] CV for $Hf_2B_2Ir_5$ shows neither oxidation nor reduction features in this potential range (Figure S2). Such conditions allow removal of the organic contaminations from the surface, accompanied with negligible dissolution of Ir from material (6.9 μg L^{-1} compared to 1.04 mg L^{-1} from metallic Ir). After 50 cycles of CV preconditioning, a current density of 10 mA cm_{geom}^{-2} can be reached at 1.59 V_{RHE} instead of 1.64 V_{RHE} from the first LSV (Figure 4), indicating that the surface of $Hf_2B_2Ir_5$ undergoes changes, leading to improved performance. These results affirm the bulk $Hf_2B_2Ir_5$ to be among the most active Ir-based electrocatalysts. In comparison, IrTe nanotubes,[59] IrCu microspheres,[60] or $SrIrO_3$ thin films deposited on $SrTiO_3$ substrates[61] reach a current density of 10 mA cm_{geom}^{-2} at potentials of 1.52, 1.512, and 1.50 V_{RHE}, respectively. It is noted that comparing such potential values would indicate the intrinsic "activity" of an electrode only if the activation processes would have reached a steady state. Neither in our case nor in the literature evidence was found that the activation is indeed in a steady-state, making such activity benchmarking a less quantitative measure than apparently indicated by the precision of the numerical values given.

The conditions of the oxygen evolution reaction (OER) are harshly oxidative and, therefore, before attributing the electrocatalytic activity to the electronic and/or structural features of the intermetallic compound, its state was carefully checked after the exposure to the reaction conditions using bulk- and surface-sensitive techniques. PXRD of the specimen after abovementioned electrochemical characterization ("LSV1/CV50/LSV2") reveals a similar pattern as before. The main difference can be attributed to slightly more pronounced peaks of the admixture phase (shown blue in Figure 2). The upward and downward variation of potentials may lead to the recrystallization of this phase, making it more detectable by XRD without, however, changing its abundance. The lattice parameters of the main $Hf_2B_2Ir_5$ phase (a = 5.6234(2) Å, b = 11.2489(3) Å, and c = 3.8307(1) Å) do not change within few e.s.d. These results reveal the bulk- and near-surface stability of the investigated material after its preconditioning. To judge the possible dissolution of constituent elements, the electrolyte after abovementioned electrochemical experiments was analyzed via inductively coupled plasma-optical emission spectroscopy (ICP-OES), showing negligible amounts of Hf (7.2 μg L^{-1}) and Ir (6.9 μg L^{-1}). Moreover, boron was not detected in the electrolyte (detection limit < 10 μg L^{-1}). Assuming the bond-breaking suggested in Figure 1, the total amount of the substance dissolved should have the component ratio Hf/B/Ir = 4:2:5, which is in agreement with the analytically found amounts of Hf and Ir (some iridium is oxidized to IrO_x and is not dissolved), and explains the results of boron analysis (expected amount—ca. 0.2 μg L^{-1}, being below the detection limit).

https://dx.doi.org/10.1021/acsaem.0c02022
ACS Appl. Energy Mater. 2020, 3, 11042−11052

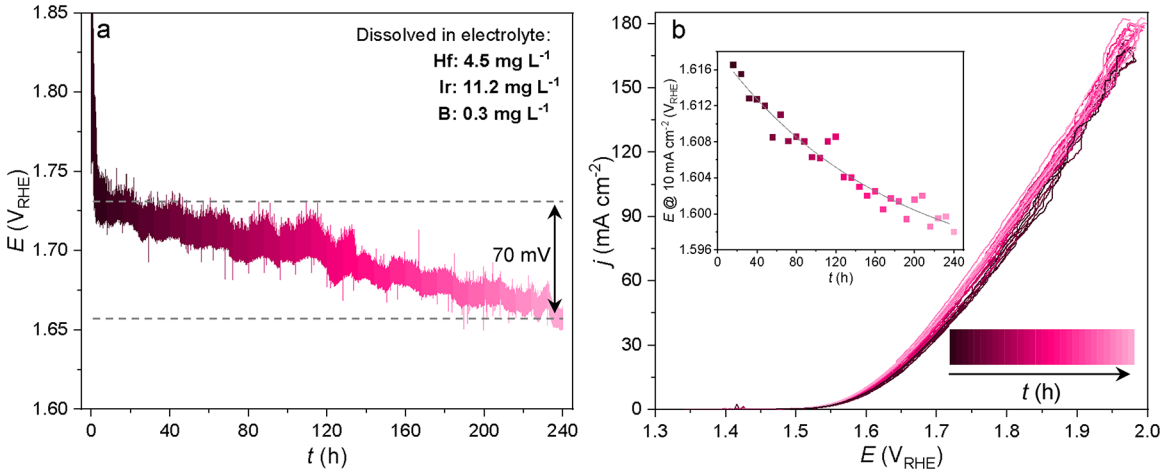

Figure 5. Long-term CP measurement with the $Hf_2B_2Ir_5$ anode material: (a) CP for 240 h at 100 mA cm_{geom}^{-2}, accompanied by (b) LSV every 8 h. Inset: the potential necessary to reach 10 mA cm^{-2}, as a function of time.

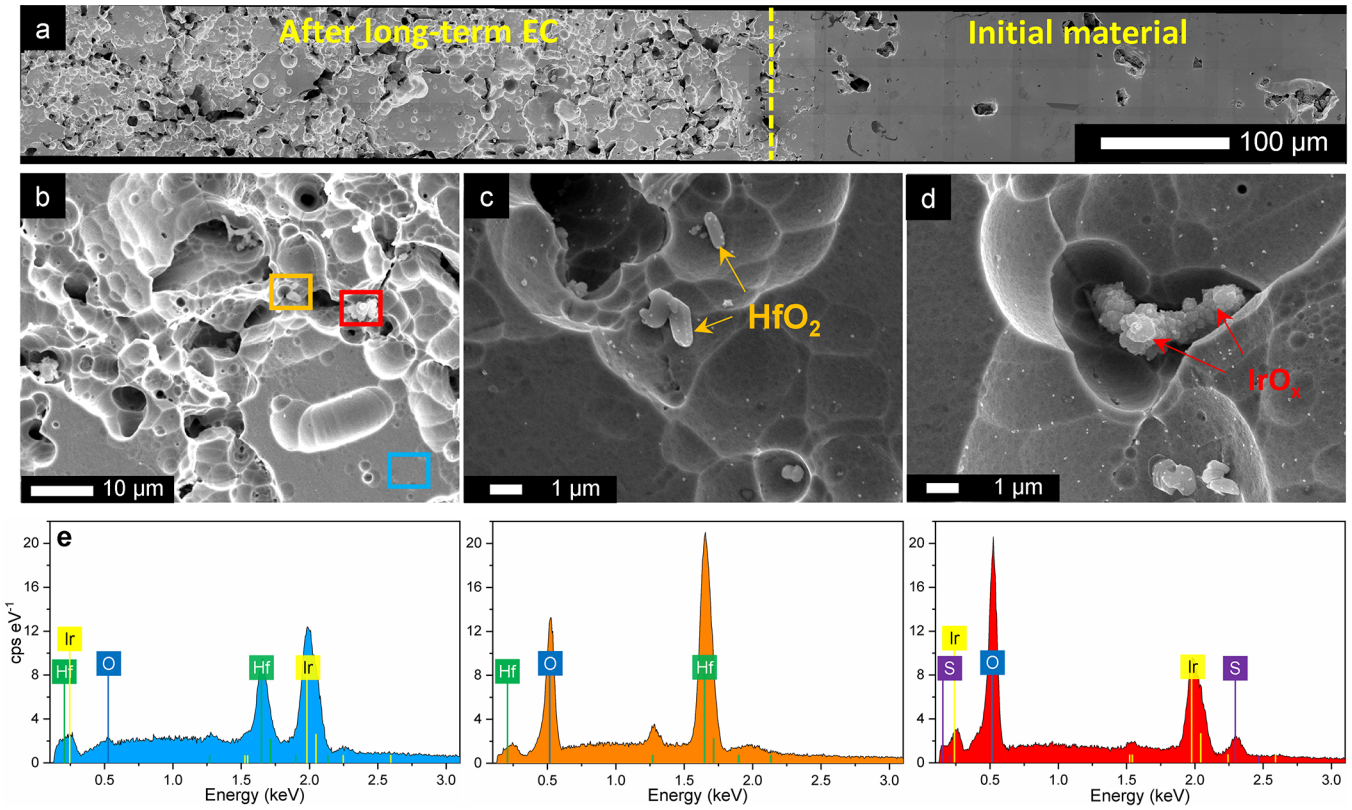

Figure 6. Microstructure of $Hf_2B_2Ir_5$ after a long-term electrochemical experiment (SEM images): (a) overview of catalyst surface from top (SE mode, 5 eV), (b) morphology of the treated area (SE, 25 kV), (c, d) Hf and Ir oxide particle agglomerates, respectively (SE, 15 kV), and (e) corresponding EDX spectra (s. colored frames in image (b)).

The ternary compound is thus a suitable candidate for a diluted form of an Ir OER catalyst. To assess its principal usefulness as a practical electrode and to better understand the phenomena of activation, a "long-term" experiment was set up. The $Hf_2B_2Ir_5$ electrocatalyst was studied using the chronopotentiometry (CP) method for 240 h, applying a current density of 100 mA cm^{-2} (Figure 5a). During 240 h, the electrode potential drops exponentially, indicating that the performance is still being continuously improved during the CP measurement, underlining the limitations of using short-term testing to measure OER activity. The fluctuations of potential values during this measurement are related to O_2 bubble detachment, which vigorously evolved during the long-term experiment. Results of LSV recorded after every 8 h (Figure 5b) confirm the electrocatalyst activation since the potential at which the electrode reaches 10 mA cm_{geom}^{-2} decreases exponentially with time (inset of Figure 5b). As a result of applied harsh conditions for extended periods of time, noticeable amounts of hafnium and iridium were found in the electrolyte after long-term CP measurement (Hf: 4.5 mg L^{-1}, Ir: 11.2 mg L^{-1}). Boron is also identified, but its amount is negligible compared to hafnium and iridium (B: 0.3 mg L^{-1}).

https://dx.doi.org/10.1021/acsaem.0c02022
ACS Appl. Energy Mater. 2020, 3, 11042−11052

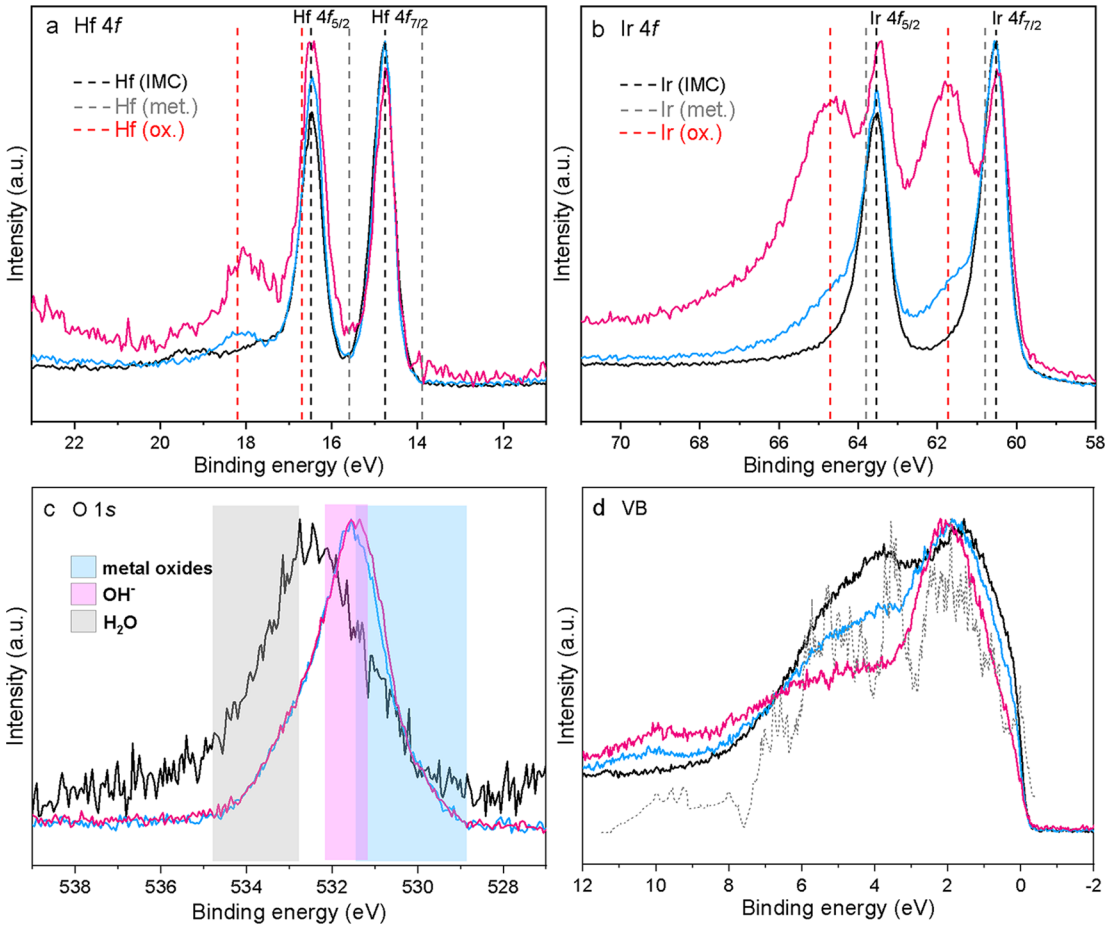

Figure 7. Normalized XPS spectra of the initial state (black), after 50 CV cycles (blue), and after long-term CP experiment (magenta) of the $Hf_2B_2Ir_5$ material. Hf 4f (a), Ir 4f (b), and O 1s (c) core levels as well as valence bands (VBs, d) are presented. The reference lines in (a) and (b) are given for intermetallic $Hf_2B_2Ir_5$ (black dashed line), elemental Hf[67] and Ir[64,69] (gray dashed lines) as well as HfO_2[68] and rutile IrO_2[58,64] (red dashed lines). Binding energy ranges for different types of oxygen species in (c) are marked in different colors. Dashed gray line on (d) represents the calculated total DOS for $Hf_2B_2Ir_5$.

The main feature of the PXRD pattern after a long-term CP experiment ("CP240") is the absence of the admixture phase (magenta in Figure 2). All reflections in the PXRD pattern were indexed with the crystallographic data of $Hf_2B_2Ir_5$, and the obtained lattice parameters (a = 5.6241(1) Å, b = 11.2503(2) Å, c = 3.8320(1) Å) are equal to those of the as-synthesized compound within few e.s.d., i.e., the bulk $Hf_2B_2Ir_5$ does not change under the OER.

Also, the SEM characterization of the material after a long-term CP experiment, accompanied by EDXS line scans (Figure S3), does not show any changes in the component ratio in the matrix of the catalyst. Nonetheless, notable changes in the morphology of the surface exposed to the electrolyte were clearly evidenced by the SEM results. To highlight the details of this morphology, reduced acceleration voltages were applied, allowing the investigation of the surface features (Figure 6a). Contrary to the morphology of the homogeneous and dense as-synthesized ternary compound, the electrochemically exposed area exhibits porosity with peculiar features. Cavities of different sizes are protruding from the subsurface layer of the $Hf_2B_2Ir_5$ specimen. This morphology can be a hint to the oxidation reaction with the transport contribution by the gaseous or liquid component. For example, such a hollow structure resembles one of hafnium diboride upon oxidation at temperatures, which are close to the boiling point of B_2O_3.[62]

The second important observation from SEM is the presence of two clearly different types of micrometer-sized particles (Figure 6b). EDX spectra revealed iridium and hafnium oxide in these particles. They are homogeneously distributed over the entire electrochemically exposed area, but at the same time, they are separated in space from each other. Both types of particles are agglomerates, 1−5 μm in size. The hafnium oxide particles are well shaped, suggesting a crystalline phase (Figure 6c). The formation of monoclinic HfO_2 during the growth of hafnium oxide films under anodization conditions is known from the literature.[63] Thinking about the possible formation route of Hf oxide, the following scenario seems appropriate: since hafnium was found in the electrolyte after a long-term experiment and the Hf^{4+} ions are the only ones known in aqueous chemistry, the saturation in the near-electrode region, accompanied by intense evolution of oxygen (as a result of the OER) leads to the continuous precipitation of the electrochemical reaction product on the electrode surface with the formation of HfO_2 grains. The agglomerates of HfO_2 crystallites are homogeneously distributed over a large electrode area, preventing the observation of its reflections in the PXRD pattern, recorded in reflection mode.

Contrary to hafnium oxide, iridium oxide particles do not crystallize but are perfectly adapted to the cavities inherent to

https://dx.doi.org/10.1021/acsaem.0c02022
ACS Appl. Energy Mater. 2020, 3, 11042−11052

the specimen surface (Figure 6d). This could suggest that they formed through the oxidation of the material at the places from which hafnium was leached. The morphology of these particles resembles those of amorphous IrO_x.[64,65] The supposed atomic arrangements on the surface (Figure 1b) allow to control the nucleation of Ir oxide (hydroxide) clusters, preventing the dissolution−precipitation and hence the formation of rutile-type IrO_2. The sulfate ions of the electrolyte can play the role of a hard template to drive the formation of a layered compound instead of the expected dense rutile structure. This is supported by the appearance of the S Kα line in the EDX spectra exclusively for amorphous-like Ir oxide particles. All of these facts suggest the formation of $IrO_x(OH)_y(SO_4)_z$ particles upon anodic treatment of the $Hf_2B_2Ir_5$ specimen. Information about Ir(III) and Ir(IV) compounds with oxo-anions (e.g., sulfate) is very scarce and mainly limited to studies in the past century,[66] emphasizing that chemistry of such compounds is far from simple and promising in terms of unexpected and extremely interesting results.

The third interesting feature is that the electrochemically treated surface is mainly composed of regions, which still maintain the initial flatness. The comparison of the Hf/Ir ratio of such areas with those of the initial $Hf_2B_2Ir_5$ material (from EDXS data) does not show any difference. Additionally, phase maps of electrochemically treated regions, obtained using electron backscatter diffraction (EBSD), reveal exclusively the $Hf_2B_2Ir_5$ phase (Figure S4). This means that the ternary compound remains unchanged not only in bulk (based on PXRD and SEM results), but also in the volume close to the surface area. This fact, in combination with the absence of the admixture phase in the PXRD pattern after a long-term CP experiment (Figure 2), indicates that the admixture phase undergoes oxidative decomposition with the formation of the iridium oxide (hydroxide, sulfate) particles, which are bound to the terminating matrix phase, boron is lost to the electrolyte and Hf oxide is deposited by dissolution and reprecipitation possibly at the hot spots of the OER, where the oxygen bubbles may support the precipitation process by local supersaturation.

X-ray photoelectron spectroscopy (XPS) was applied to investigate the surface electronic state of the electrocatalyst. The Hf 4f, Ir 4f, and O 1s regions of XPS spectra were recorded before and after the electrochemical experiments (Figure 7a−c). The Hf 4f and Ir 4f core levels measurements for as-synthesized $Hf_2B_2Ir_5$ material reveal the expected characteristics of the IMC. The doublet of the Hf 4f core levels (including Hf $4f_{5/2}$ at 16.5 eV and Hf $4f_{7/2}$ at 14.8 eV) is located between the corresponding doublets of the metallic hafnium (15.6 and 13.9 eV, respectively)[67] and hafnium oxide HfO_2 (18.2 and 16.7 eV),[68] in agreement with a strong charge transfer from Hf to the B−Ir polyanion (QTAIM charge $Hf^{+1.83}$).[53] The Ir 4f core levels (Ir $4f_{5/2}$ at 63.6 eV and Ir $4f_{7/2}$ at 60.5 eV) are slightly (0.2 eV) shifted toward lower binding energies compared to metallic iridium (63.8 and 60.8 eV),[64,69] and far away (1.1 eV) from the core levels of rutile-type iridium(IV) oxide (64.7 and 61.7 eV).[58,64] This finding correlates well with the negative QTAIM charge of Ir (−0.63 to −0.66).[53] Such shifts emphasize the expected modification of the electronic structure of an IMC with strong directed interactions as compared to a hypothetical substitutional alloy. According to these XPS data, Hf donates electrons to other constituents of the compound and becomes partially positively charged, which is also in line with the relative electronegativities of the elements (Hf: 1.3, Ir: 2.20, and B: 2.04)[70] and chemical bonding analysis.[53] The XPS data of the B 1s core level are not conclusive due to a quite weak peak because of a low relative sensitivity factor (RSF) of the B 1s orbital and the simultaneous presence of the heavy elements with high RSFs (Figure S5a).[37] Nevertheless, the peak at 188.2 eV in the XPS spectra of the pristine sample (Figure S5a) belongs to the B 1s core level and is shifted toward higher binding energies, compared to elemental boron (186.4−186.5 eV).[71] This indicates a partial positive charge of boron in $Hf_2B_2Ir_5$, donating electrons to the iridium atoms, in line with chemical bonding analysis (Figure 1).

A comparison of the XPS data for specimens before and after different electrochemical treatments clearly reveals the dominant presence of the IMC phase (Figure 7a,b), supporting the concept of remarkable stability of the metallic matrix phase. A progressive increase in the oxidized forms for iridium and hafnium after the CV and even more pronounced after long-term CP experiment follows from the formation of the active Ir phase and the presence of precipitated Hf oxide identified in the morphological analysis. The Hf 4f XPS spectra consist of at least two components: (i) the intermetallic part, which remains almost unchanged in terms of binding energies and peak widths, and (ii) the oxide part, which is presented by an additional peak at ∼18.1 eV that is increasing with time of electrochemical treatment. This oxide peak is significantly broader and represents the Hf $4f_{5/2}$ part of the HfO_2 doublet, whereas the Hf $4f_{7/2}$ peak is overlapping with the peak of the intermetallic Hf $4f_{5/2}$, leading to an increase in the width of the latter one and a change of the intensity ratio between the lines in the Hf 4f main doublet (Figure 7a). The identification of Ir oxide is more pronounced due to its presence as a highly dispersed species, compared to hafnium existing as well-developed crystals with obviously lower surface coverage, and is represented by peaks at binding energies of 64.7 and 61.7 eV. The asymmetric shape of the oxide peaks is in good agreement with previously reported XPS data on iridium oxides.[18,64,72]

The formation of the oxidized particles is also evidenced by the shift of the O 1s core level (Figure 7c) from the region of adsorbed water (∼533 eV)[58,69] toward the hydroxide region (various OH^- species at 531.0−531.5 eV).[69] The signal is broad and has shoulders on both sides, allowing to conclude the presence of adsorbed water as well as the contribution of the lattice oxygen of the oxide. Nevertheless, the ratio between hydroxide/oxide is very large, indicating a dominant presence of hydroxyl groups on the surface. It is also important to notice that the O 1s spectrum remains almost unchanged after the initial CV treatment.

The measured valence band of the as-synthesized $Hf_2B_2Ir_5$ (Figure 7d) reflects the calculated density of states (DOS) for this ternary compound (Figure 7d). The broad valence band (approximately 8.0 eV) originated from Ir 5d states with an admixture of Hf 5d and B 2p electrons (based on DOS calculations).[53] The features of experimental valence bands (VBs) also clearly alter upon electrochemical treatments (Figure 7d). The contribution in the range from 3 to 8 eV reduces significantly, whereas the intensity in the region closer to Fermi edge remains unchanged with a slight shift to higher binding energies. Such flattening in the region of 3−8 eV is inherent for experimentally observed and calculated valence bands of IrO_2.[73] Additionally, contribution at high binding energies (8−12 eV) increases with the duration of the

https://dx.doi.org/10.1021/acsaem.0c02022
ACS Appl. Energy Mater. 2020, 3, 11042−11052

electrochemical experiment. The reduction in the intensity of the Fermi edge (Figure 7d) is due to the coverage of the surface with hydroxide species. Their presence, even after a prolonged OER, puts in evidence the functioning of the concept of activating a metallic matrix so that a very thin (information depth of lab XPS) oxidic surface layer stays electrically well connected to the bulk of the electrode. This allows the transport of stoichiometric amounts of charge carriers despite the presence of an oxide, which is necessary to bind the reactant water molecules to the active surface.

The oxidized Ir mostly originates from the oxidation of secondary phases, the disappearance of which after the long-term CP experiment was confirmed by the PXRD and SEM results (Figures 2 and 6). A number of other arguments support the bulk stability of $Hf_2B_2Ir_5$ under harsh OER conditions: (i) the position of Ir $4f_{5/2}$ and Ir $4f_{7/2}$ core levels do not change (compared to the as-prepared intermetallic compound) after different electrochemical treatments, while the oxidic contribution appears additionally and increases with the time of the electrochemical treatment (Figure 7b); (ii) the surface is porous, but a lot of flat areas with the composition identical to that of the as-prepared material can be recognized after 240 h of CP (Figure 6a); (iii) the chemical bonding analysis of $Hf_2B_2Ir_5$ clearly reveals the possibility of Hf leaching due to a pronounced ionic interaction between the Hf atoms and the Ir−B polyanion, whereas the removal of Ir from the Ir−B network will be energetically unfavorable. Furthermore, gradual improvement of the OER activity with time of the CP can be described as an exponential function of time, showing the "saturation" of the OER activity after a certain time of operation, showing the self-improvement of the electrocatalyst due to the availability of easily oxidized secondary phases and bulk integrity of the $Hf_2B_2Ir_5$ itself. In general, the unchanged onset of the OER accompanied by the gradual increase of the current densities at the same potential values point out the combined function of ternary compound $Hf_2B_2Ir_5$ and $IrO_x(OH)_y(SO_4)_z$, formed mainly as a result of the oxidative decomposition of secondary phases.

CONCLUSIONS

The ternary intermetallic compound $Hf_2B_2Ir_5$ was investigated as an electrocatalyst for the anodic reaction of water splitting. The harsh oxidative conditions of the OER activate the bulk-stable IMC by self-limited changes on the surface of the investigated material. The OER performance can be related to the activity of the Ir termination of the ternary compound itself, supported by the activity of agglomerated particles of $IrO_x(OH)_y(SO_4)_z$. The latter mainly results from the oxidation of secondary phases in addition to self-controlled near-surface oxidation of $Hf_2B_2Ir_5$. The chemical bonding features of the $Hf_2B_2Ir_5$ compound with a cage-like Ir−B framework, hosting Hf atoms, inhibit deep Ir leaching, and control the oxidation process. As a result, a self-optimized composite of $Hf_2B_2Ir_5$ and $IrO_x(OH)_y(SO_4)_z$ catalyze the evolution of oxygen over 240 h at relatively high current densities of 100 mA cm^{-2}. In other words, the intermetallic compound $Hf_2B_2Ir_5$ with a well-defined cage-like structure is not only an active OER electrocatalyst by itself but is also a support structure for self-optimized formation of OER-active $IrO_x(OH)_y(SO_4)_z$ particles as a second-generation catalyst. By optimizing the relationship between the stable and active matrix and secondary precursor of similar chemical composition, one can obtain an optimal dispersion of the active Ir compound with a strong chemical link to the stable metallic support structure. We anticipate that such a concept of cooperative phases with different chemical stabilities under the OER might be generalized to other systems and hence become an avenue to materials allowing to replace Ir with albeit a reduction in performance, but at sustained operational stability. One may learn from this work that the attempt to replace the Ir oxide by a single compound of hypothetical electronic structure is a less promising way forward compared to the present strategy of dividing the different functions of activity and stability between several phases with a similar chemical composition.

ASSOCIATED CONTENT

Supporting Information

The Supporting Information is available free of charge at https://pubs.acs.org/doi/10.1021/acsaem.0c02022.

Additional figures, e.g., metallography of as-synthesized $Hf_2B_2Ir_5$; cyclic voltammetry of $Hf_2B_2Ir_5$ and metallic Ir working electrodes; preliminary SEM characterization and EBSD phase map of $Hf_2B_2Ir_5$ specimen after long-term CP experiment; and B 1s and S 2p XPS core levels spectra of $Hf_2B_2Ir_5$ after different electrochemical treatments (PDF)

AUTHOR INFORMATION

Corresponding Authors

Yuri Grin − *Max-Planck-Institut für Chemische Physik fester Stoffe, 01187 Dresden, Germany;* orcid.org/0000-0003-3891-9584; Email: grin@cpfs.mpg.de

Iryna Antonyshyn − *Max-Planck-Institut für Chemische Physik fester Stoffe, 01187 Dresden, Germany;* orcid.org/0000-0002-7652-0630; Email: Iryna.Antonyshyn@cpfs.mpg.de

Authors

Ana M. Barrios Jiménez − *Max-Planck-Institut für Chemische Physik fester Stoffe, 01187 Dresden, Germany*

Ulrich Burkhardt − *Max-Planck-Institut für Chemische Physik fester Stoffe, 01187 Dresden, Germany*

Raul Cardoso-Gil − *Max-Planck-Institut für Chemische Physik fester Stoffe, 01187 Dresden, Germany*

Katharina Höfer − *Max-Planck-Institut für Chemische Physik fester Stoffe, 01187 Dresden, Germany*

Simone G. Altendorf − *Max-Planck-Institut für Chemische Physik fester Stoffe, 01187 Dresden, Germany*

Robert Schlögl − *Fritz-Haber-Institut der Max-Planck-Gesellschaft, 14195 Berlin, Germany; Max-Planck-Institut für Chemische Energiekonversion, 45470 Mülheim an der Ruhr, Germany*

Complete contact information is available at: https://pubs.acs.org/10.1021/acsaem.0c02022

Funding

Max-Planck-Society.

Notes

The authors declare no competing financial interest.

ACKNOWLEDGMENTS

The authors thank Dr. Olga Sichevych and Sever Flipo (sample synthesis), Dr. Igor Veremchuk (sample densification via SPS technique), Sylvia Kostmann (metallographic preparation and light microscopy), Petra Scheppan (EDXS analysis and SEM), Stefan Hückmann (Guinier powder X-ray diffraction measure-

ments), Anja Völzke, Ulrike Schmidt, and Dr. Gudrun Auffermann (elemental analysis via ICP-OES), and Geralf Timm and Jörg Faltin (manufacturing of the electrochemical cell).

■ ABBREVIATIONS

BSE, backscattered electron
CP, chronopotentiometry
CV, cyclic voltammetry
DOS, density of states
EBSD, electron backscattered diffraction
EDXS, energy-dispersive X-ray spectroscopy
E_{max}, maximum potential
e.s.d., estimated standard deviation
HER, hydrogen evolution reaction
HOR, hydrogen oxidation reaction
H_{UPD}, hydrogen underpotential deposition
ICP-OES, inductively coupled plasma-optical emission spectrometry
IMC, intermetallic compound
j, current density
LSV, linear sweep voltammetry
OER, oxygen evolution reaction
ORR, oxygen reduction reaction
PEM, proton exchange membrane
PXRD, powder X-ray diffraction
QTAIM, quantum theory of atoms in molecules
RHE, reference hydrogen electrode
SE, secondary electron
SEM, scanning electron microscopy
SPS, spark plasma sintering
VB, valence band
WDXS, wavelength-dispersive X-ray spectroscopy
XPS, X-ray photoelectron spectroscopy

■ REFERENCES

(1) Schlögl, R. Sustainable energy systems: the strategic role of chemical energy conversion. *Top Catal.* **2016**, *59*, 772−786.
(2) Chu, S.; Cui, Y.; Liu, N. The path towards sustainable energy. *Nat. Mater.* **2016**, *16*, 16−22.
(3) Lanzafame, P.; Abate, S.; Ampelli, C.; Genovese, C.; Passalacqua, R.; Centi, G.; Perathoner, S. Beyond solar fuels: renewable energy-driven chemistry. *ChemSusChem* **2017**, *10*, 4409−4419.
(4) *Hydrogen Economy. Supply Chain, Life Cycle Analysis and Energy Transition for Sustainability*; Scipioni, A.; Manzardo, A.; Ren, J., Eds.; Academic Press, Elsevier, 2017.
(5) Dincer, I.; Acar, C. Smart energy solutions with hydrogen options. *Int. J. Hydrogen Energy* **2018**, *43*, 8579−8599.
(6) Staffell, I.; Scamman, D.; Velazquez Abad, A.; Balcombe, P.; Dodds, P. E.; Ekins, P.; Shah, N.; Ward, K. R. The role of hydrogen and fuel cells in the global energy system. *Energy Environ. Sci.* **2019**, *12*, 463−491.
(7) Carmo, M.; Fritz, D. L.; Mergel, J.; Stolten, D. A comprehensive review on PEM water electrolysis. *Int. J. Hydrogen Energy* **2013**, *38*, 4901−4934.
(8) Schalenbach, M.; Zeradjanin, A. R.; Kasian, O.; Cherevko, S.; Mayrhofer, K. J. J. A perspective on low-temperature water electrolysis − challenges in alkaline and acidic technology. *Int. J. Electrochem. Sci.* **2018**, *13*, 1173−1226.
(9) Koper, M. T. M. Thermodynamic theory of multi-electron transfer reactions: implications for electrocatalysis. *J. Electroanal. Chem.* **2011**, *660*, 254−260.
(10) Reier, T.; Nong, H. N.; Teschner, D.; Schlögl, R.; Strasser, P. Electrocatalytic oxygen evolution reaction in acidic environments − reaction mechanism and catalysis. *Adv. Energy Mater.* **2017**, *7*, No. 1601275.
(11) Seh, Z. W.; Kibsgaard, J.; Dickens, C. F.; Chorkendorff, I.; Nørskov, J. K.; Jaramillo, T. F. Combining theory and experiment in electrocatalysis: insights into material design. *Science* **2017**, *355*, No. eaad4998.
(12) Fabbri, E.; Schmidt, T. J. Oxygen evolution reaction − the enigma in water electrolysis. *ACS Catal.* **2018**, *8*, 9765−9774.
(13) Pourboix, M. *Atlas of Electrochemical Equilibria in Aqueous Solutions*; NACE International Cebelcor: Texas, 1974.
(14) Minguzzi, A.; Fan, F.-R. F.; Vertova, A.; Rondinini, S.; Bard, A. J. Dynamic potential-pH diagrams application to electrocatalysts for water oxidation. *Chem. Sci.* **2012**, *3*, 217−229.
(15) Reier, T.; Oezaslan, M.; Strasser, P. Electrocatalytic oxygen evolution reaction (OER) on Ru, Ir, and Pt catalysts: a comparative study of nanoparticles and bulk materials. *ACS Catal.* **2012**, *2*, 1765−1772.
(16) Danilovic, N.; Subbaraman, R.; Chang, K.-C.; Chang, S. H.; Kang, Y. J.; Snyder, J.; Paulikas, A. P.; Strmcnik, D.; Kim, Y.-T.; Myers, D.; Stamenkovic, V. R.; Markovic, N. M. Activity-stability trends for the oxygen evolution reaction on monometallic oxides in acidic environments. *J. Phys. Chem. Lett.* **2014**, *5*, 2474−2478.
(17) Cherevko, S.; Zeradjanin, A. R.; Topalov, A. A.; Kulyk, N.; Katsounaros, I.; Mayrhofer, K. J. J. Dissolution of noble metals during oxygen evolution in acidic media. *ChemCatChem* **2014**, *6*, 2219−2223.
(18) Pfeifer, V.; Jones, T. E.; Velasco Vélez, J. J.; Massué, C.; Greiner, M. T.; Arrigo, R.; Teschner, D.; Girgsdies, F.; Scherzer, M.; Allan, J.; Hashagen, M.; Weinberg, G.; Piccinin, S.; Hävecker, M.; Knop-Gericke, A.; Schlögl, R. The electronic structure of iridium oxide electrodes active in water splitting. *Phys. Chem. Chem. Phys.* **2016**, *18*, 2292−2296.
(19) Cherevko, S.; Geiger, S.; Kasian, O.; Mingers, A.; Mayrhofer, K. J. J. Oxygen evolution activity and stability of iridium in acidic media. Part 1. − Metallic iridium. *J. Electroanal. Chem.* **2016**, *773*, 69−78.
(20) Cherevko, S.; Geiger, S.; Kasian, O.; Mingers, A.; Mayrhofer, K. J. J. Oxygen evolution activity and stability of iridium in acidic media. Part2. − Electrochemically grown hydrous iridium oxide. *J. Electroanal. Chem.* **2016**, *774*, 102−110.
(21) Pfeifer, V.; Jones, T. E.; Wrabetz, S.; Massué, C.; Velasco Vélez, J. J.; Arrigo, R.; Scherzer, M.; Piccinin, S.; Hävecker, M.; Knop-Gericke, A.; Schlögl, R. Reactive oxygen species in iridium-based OER catalysts. *Chem. Sci.* **2016**, *7*, 6791−6795.
(22) Geiger, S.; Kasian, O.; Shrestha, B. R.; Mingers, A. M.; Mayrhofer, K. J. J.; Cherevko, S. Activity and stability of electrochemically and thermally treated iridium for the oxygen evolution reaction. *J. Electrochem. Soc.* **2016**, *163*, F3132−F3138.
(23) Özer, E.; Spöri, C.; Reier, T.; Strasser, P. Iridium (111), iridium (110), and ruthenium (0001) single crystals as model catalysts for the oxygen evolution reaction: insights into the electrochemical oxide formation and electrocatalytic activity. *ChemCatChem* **2017**, *9*, 597−603.
(24) Jensen, A. W.; Sievers, G. W.; Jensen, K. D.; Quinson, J.; Arminio Ravelo, J. A.; Brüser, V.; Arenz, M.; Escudero Escribano, M. Self-supported nanostructures iridium-based networks as highly active electrocatalysts for oxygen evolution in acidic media. *J. Mater. Chem. A* **2020**, *8*, 1066−1071.
(25) Nørskov, J. K.; Bligaard, T.; Rossmeisl, J.; Christensen, C. H. Towards the computational design of solid catalysts. *Nat. Chem.* **2009**, *1*, 37−46.
(26) Xin, H.; Vojvodic, A.; Voss, J.; Nørskov, J. K.; Abild-Pedersen, F. Effects of *d*-band shape on the surface reactivity of transition-metal alloys. *Phys. Rev. B* **2014**, *89*, No. 115114-1.
(27) Medford, A. J.; Vojvodic, A.; Hummelshøj, J. S.; Voss, J.; Abild-Pedersen, F.; Studt, F.; Bligaard, T.; Nilsson, A.; Nørskov, J. K. From the Sabatier principle to a predictive theory of transition-metal heterogeneous catalysis. *J. Catal.* **2015**, *328*, 36−42.

https://dx.doi.org/10.1021/acsaem.0c02022
ACS Appl. Energy Mater. 2020, 3, 11042−11052

(28) Armbrüster, M.; Schlögl, R.; Grin, Y. Intermetallic compounds in heterogeneous catalysis − a quickly developing field. *Sci. Technol. Adv. Mater.* **2014**, *15*, No. 034803.
(29) Tsai, A.-P.; Kameoka, S.; Nozawa, K.; Shimoda, M.; Ishii, Y. Intermetallic: a pseudoelement for catalysis. *Acc. Chem. Res.* **2017**, *50*, 2879−2885.
(30) Rö*ß*ner, L.; Armbrüster, M. Electrochemical energy conversion on intermetallic compounds: a review. *ACS Catal.* **2019**, *9*, 2018−2062.
(31) Armbrüster, M. Intermetallic compounds in catalysis − a versatile class of materials meets interesting challenges. *Sci. Technol. Adv. Mater.* **2020**, *21*, 303−322.
(32) Mondschein, J. S.; Kumar, K.; Holder, C. F.; Seth, K.; Kim, H.; Schaak, R. E. Intermetallic Ni_2Ta electrocatalyst for the oxygen evolution reaction in highly acidic electrolytes. *Inorg. Chem.* **2018**, *57*, 6010−6015.
(33) Antonyshyn, I.; Barrios Jiménez, A. M.; Sichevych, O.; Burkhardt, U.; Veremchuk, I.; Schmidt, M.; Ormeci, A.; Spanos, I.; Tarasov, A.; Teschner, D.; Algara-Siller, G.; Schlögl, R.; Grin, Y. Al_2Pt for oxygen evolution in water splitting: a strategy for creating multifunctionality in electrocatalysis. *Angew. Chem., Int. Ed.* **2020**, *59*, 16770−16776.
(34) *Binary Alloy Phase Diagrams*; Massalski, T. B., Ed.; ASM International: Materials Park, 1990.
(35) Chisaka, M.; Sasaki, H.; Muramoto, H. Monoclinic hafnium oxynitride supported on reduced graphene oxide to catalyse the oxygen reduction reaction in acidic media. *Phys. Chem. Chem. Phys.* **2014**, *16*, 20415−20419. and references therein.
(36) Yang, X.; Zhao, F.; Yeh, Y.-W.; Selinsky, R. S.; Chen, Z.; Yao, N.; Tully, C. G.; Ju, Y.; Koel, B. E. Nitrogen-plasma treated hafnium oxyhydroxide as an efficient acid-stable electrocatalyst for hydrogen evolution and oxidation reactions. *Nat. Commun.* **2019**, *10*, No. 1543.
(37) Mazánek, V.; Nahdi, H.; Luxa, J.; Sofer, Z.; Pumera, M. Electrochemistry of layered metal diborides. *Nanoscale* **2018**, *10*, 11544−11552.
(38) Sitler, S. J.; Raja, K. S.; Charit, I. Metal-rich transition metal diborides as electrocatalysts for hydrogen evolution reactions in a wide range of pH. *J. Electrochem. Soc.* **2016**, *163*, H1069−H1075.
(39) Stojić, D. L.; Kumrić, S. V.; Grozdić, T. D.; Koteski, V. J.; Cekić, B. D. Hydrogen production and storage − investigation of Hf-based intermetallics. *J. Power Sources* **2009**, *193*, 165−169.
(40) Kugai, L. N.; Nazarchuk, T. N. Chemical stability of diborides of the transition metals from groups IV-V of the periodic system. *Poroshk. Metall.* **1971**, *3*, 51−55.
(41) Masa, J.; Weide, P.; Peeters, D.; Sinev, I.; Xia, W.; Sun, Z.; Somsen, C.; Muhler, M.; Schumann, W. Amorphous cobalt boride (Co_2B) as a highly efficient nonprecious catalyst for electrochemical water splitting: oxygen and hydrogen evolution. *Adv. Energy Mater.* **2016**, *6*, No. 1502313.
(42) Vij, V.; Sultan, S.; Harzandi, A. M.; Meena, A.; Tiwari, J. N.; Lee, W.-G.; Yoon, T.; Kim, K. S. Nickel-based electrocatalysts for energy-related applications: oxygen reduction, oxygen evolution, and hydrogen evolution reactions. *ACS Catal.* **2017**, *7*, 7196−7225. and references therein.
(43) Gupta, S.; Patel, N.; Fernandes, R.; Hanchate, S.; Miotello, A.; Kothari, D. C. Co-Mo-B nanoparticles as a non-precious and efficient bifunctional electrocatalyst for hydrogen and oxygen evolution. *Electrochim. Acta* **2017**, *232*, 64−71.
(44) Hao, W.; Wu, R.; Zhang, R.; Ha, Y.; Chen, Z.; Wang, L.; Yang, Y.; Ma, X.; Sun, D.; Fang, F.; Guo, Y. Electroless plating of highly efficient bifunctional boride-based electrodes toward practical overall water splitting. *Adv. Energy Mater.* **2018**, *8*, No. 1801372.
(45) Masa, J.; Andronescu, C.; Antoni, H.; Sinev, I.; Seisel, S.; Elumeeva, K.; Barwe, S.; Marti-Sanchez, S.; Arbiol, J.; Roldan Cuenya, B.; Muhler, M.; Schuhmann, W. Role of boron and phosphorus in enhanced electrocatalytic oxygen evolution by nickel borides and nickel phosphides. *ChemElectroChem* **2019**, *6*, 235−240. and references therein.
(46) Gupta, S.; Patel, M. K.; Miotello, A.; Patel, N. Metal boride-based catalysts for electrochemical water-splitting: a review. *Adv. Funct. Mater.* **2019**, No. 1906481.
(47) Gupta, S.; Jadhav, H.; Sinha, S.; Miotello, A.; Patel, M. K.; Sarkar, A.; Patel, N. Cobalt-boride nanostructured thin films with high performance and stability for alkaline water oxidation. *ACS Sustainable Chem. Eng.* **2019**, *7*, 16651−16658.
(48) Guo, F.; Wu, Y.; Chen, H.; Liu, Y.; Yang, L.; Ai, X.; Zou, X. High-performance oxygen evolution electrocatalysis by boronized metal sheets with self-functionalized surfaces. *Energy Environ. Sci.* **2019**, *12*, 684−692.
(49) Wygant, B. R.; Kawashima, K.; Buddie Mullins, C. Catalyst or precatalyst? The effect of oxidation on transition metal carbide, pnictide, and chalcogenide oxygen evolution catalysts. *ACS Energy Lett.* **2018**, *3*, 2956−2966.
(50) Masa, J.; Schuhmann, W. The role of non-metallic and metalloid elements on the electrocatalytic activity of cobalt and nickel catalysts for the oxygen evolution reaction. *ChemCatChem* **2019**, *11*, 5842−5854.
(51) *WinXPOW, Version 2.25*; STOE and Cie GmbH: Darmstadt, Germany, 2009.
(52) Akselrud, L.; Grin, Yu WinCSD: software package for crystallographic calculations (Version 4). *J. Appl. Crystallogr.* **2014**, *47*, 803−805.
(53) Sichevych, O.; Flipo, S.; Ormeci, A.; Bobnar, M.; Akselrud, L.; Prots, Y.; Burkhardt, U.; Gumeniuk, R.; Leithe-Jasper, A.; Grin, Yu Crystal structure and physical properties of the cage compound $Hf_2Ir_{5+\delta}B_{2-2\delta}$. *Inorg. Chem.* **2020**, *59*, No. 14280.
(54) Rogl, P. The crystal structure of $ZrIr_3B_{\sim 4}$. *Acta Crystallogr. B* **1978**, *34*, 721−724.
(55) Rogl, P.; Nowotny, H. Studies of the (Sc, Zr, Hf)-(Rh, Ir)-B systems. *J. Less-Common Met.* **1979**, *67*, 41−50.
(56) Spanos, I.; Auer, A. A.; Neugebauer, S.; Deng, X.; Tüysüz, H.; Schlögl, R. Standardized benchmarking of water splitting catalysts in a combined electrochemical flow cell/inductively coupled plasma-optical emission spectrometry (ICP-OES) setup. *ACS Catal.* **2017**, *7*, 3768−3778.
(57) Anantharaj, S.; Ede, S. R.; Karthick, K.; Sam Sankar, S.; Sangeetha, K.; Karthik, P. E.; Kundu, S. Precision and correctness in the evaluation of electrocatalytic water splitting: revisiting activity parameters with a critical assessment. *Energy Environ. Sci.* **2018**, *11*, 744−771.
(58) Saveleva, V. A.; Wang, L.; Teschner, D.; Jones, T.; Gago, A. S.; Friedrich, K. A.; Zafeiratos, S.; Schlögl, R.; Savinova, E. R. Operando evidence for a universal oxygen evolution mechanism on thermal and electrochemical iridium oxides. *J. Phys. Chem. Lett.* **2018**, *9*, 3154−3160.
(59) Shi, Q.; Zhu, C.; Du, D.; Wang, J.; Xia, H.; Engelhard, M. H.; Feng, S.; Lin, Y. Ultrathin dendritic IrTe nanotubes for an efficient oxygen evolution reaction in a wide pH range. *J. Mater. Chem. A* **2018**, *6*, 8855−8859.
(60) Liu, X.; Li, Z.; Zhou, L.; Wang, K.; Zhao, X.; Li, Q.; Deng, Y. Facile synthesis of IrCu microspheres based on polyol method and study on their electro-catalysis performances to oxygen evolution reaction. *Nanomaterials* **2019**, *9*, No. 1145.
(61) Seitz, L. C.; Dickens, C. F.; Nishio, K.; Hikita, Y.; Montoya, J.; Doyle, A.; Kirk, C.; Vojvodic, A.; Hwang, H. Y.; Norskov, J. K.; Jaramillo, T. F. A highly active and stable $IrO_x/SrIrO_3$ catalyst for the oxygen evolution reaction. *Science* **2016**, *353*, 1011−1013.
(62) Bargeron, C. B.; Benson, R. C.; Newman, R. W.; Jette, A. N.; Phillips, T. E. Oxidation mechanisms of hafnium carbide and hafnium diboride in the temperature range 1400 to 2100 °C. *Johns Hopkins APL Tech. Dig.* **1993**, *14*, 29−36.
(63) Mozalev, A.; Bendova, M.; Gispert-Guirado, F.; Llobet, E. Hafnium-oxide 3-D nanofilms via the anodizing of Al/Hf metal layers. *Chem. Mater.* **2018**, *30*, 2694−2708.
(64) Pfeifer, V.; Jones, T. E.; Velasco Vélez, J. J.; Massué, C.; Arrigo, R.; Teschner, D.; Girgsdies, F.; Scherzer, M.; Greiner, M. T.; Allan, J.; Hashagen, M.; Weinberg, G.; Piccinin, S.; Hävecker, M.; Knop-

https://dx.doi.org/10.1021/acsaem.0c02022
ACS Appl. Energy Mater. 2020, 3, 11042−11052

Gericke, A.; Schlögl, R. The electronic structure of iridium and its oxides. *Surf. Interface Anal.* **2016**, *48*, 261−273.
(65) Ruiz Esquius, J.; Morgan, D. J.; Spanos, I.; Hewes, D. G.; Freakley, S. J.; Hutchings, G. J. Effect of base on the facile hydrothermal preparation of highly active IrO_x oxygen evolution catalysts. *ACS Appl. Energy Mater.* **2020**, *3*, 800−809.
(66) Malatesta, L. Some Recent Aspects of the Chemistry of Iridium. *Fascilicus extraodinarius Alfred Werner, 1866-1919*; Werner, A., Ed.; Verlag Helvetica Chimica Acta: Basel, 1967.
(67) Arranz, A.; Palacio, C. Core level spectra of hafnium and hafnium nitride ($HfN_{0.9}$) by XPS. *Surf. Sci. Spectra* **2004**, *11*, 33−42.
(68) Barreca, D.; Milanov, A.; Fischer, R. A.; Devi, A.; Tondello, E. Hafnium oxide thin film grown by ALD: an XPS study. *Surf. Sci. Spectra* **2007**, *14*, 34−40.
(69) Reier, T.; Teschner, D.; Lunkenbein, T.; Bergmann, A.; Selve, S.; Karehnert, R.; Schlögl, R.; Strasser, P. Electrocatalytic oxygen evolution on iridium oxide: uncovering catalyst-substrate interactions and active iridium oxide species. *J. Electrochem. Soc.* **2014**, *161*, F876−F882.
(70) *The Elements*; Emsley, J., Ed.; Clarendon Press: Oxford, 1998.
(71) Schreifels, J. A.; Maybury, P. C.; Swartz, W. E. X-ray photoelectron spectroscopy of nickel boride catalysts: correlation of surface states with reaction products in the hydrogenation of acrylonitrile. *J. Catal.* **1980**, *65*, 195−206.
(72) Johnson, B.; Ranjan, C.; Greiner, M.; Arrigo, R.; Schuster, M. E.; Höpfner, B.; Gorgoi, M.; Lauermann, I.; Willinger, M.; Knop-Gericke, A.; Schlögl, R. Characterization of platinum and iridium oxyhydrate surface layers from platinum and iridium foils. *ChemSusChem* **2016**, *9*, 1634−1646.
(73) Ping, Y.; Galli, G.; Goddard, W. A. Electronic structure of IrO_2: the role of the metal d orbitals. *J. Phys. Chem. C* **2015**, *119*, 11570−11577.

https://dx.doi.org/10.1021/acsaem.0c02022
ACS Appl. Energy Mater. 2020, 3, 11042−11052